Short-Term Synaptic Dynamics Control the Activity Phase of Neurons in an Oscillatory Network

Abbreviated Title: Synaptic dynamics influence activity phase of oscillatory neurons

Authors: Diana Martinez[1*], Haroon Anwar[1], Amitabha Bose[2], Dirk Bucher[1], Farzan Nadim[1,2]

1 Federated Department of Biological Sciences, New Jersey Institute of Technology and Rutgers University, Newark, NJ 07102.

2 Department of Mathematical Sciences, New Jersey Institute of Technology, Newark, NJ 07102.

* Current Address: Department of Biomedical Sciences and Dalton Cardiovascular Research Center, University of Missouri, 134 Research Park Dr., Columbia, MO 65211, USA

Corresponding Author: Farzan Nadim, New Jersey Institute of Technology, Department of Biological Sciences, 323 Martin Luther King Blvd, Newark, NJ 07102, Phone (973) 596-8453, Email: farzan@njit.edu

Abstract

In oscillatory systems, neuronal activity phase is often independent of network frequency. Such phase maintenance requires adjustment of synaptic input with network frequency, a relationship that we explored using the crab, *Cancer borealis*, pyloric network. The burst phase of pyloric neurons is relatively constant despite a >2-fold variation in network frequency. We used noise input to characterize how input shape influences burst delay of a pyloric neuron, and then used dynamic clamp to examine how burst phase depends on the period, amplitude, duration, and shape of rhythmic synaptic input. Phase constancy across a range of periods required a proportional increase of synaptic duration with period. However, phase maintenance was also promoted by an increase of amplitude and peak phase of synaptic input with period. Mathematical analysis shows how short-term synaptic plasticity can coordinately change amplitude and peak phase to maximize the range of periods over which phase constancy is achieved.

150/150

Introduction

Oscillatory neural activity is often organized into different phases across groups of neurons, both in brain rhythms associated with cognitive tasks or behavioral states (Hasselmo et al., 2002; Buzsaki and Wang, 2012; Buzsaki and Tingley, 2018), and in central pattern generating (CPG) circuits that drive rhythmic motor behaviors (Marder and Bucher, 2001; Marder et al., 2005; Grillner, 2006; Bucher et al., 2015; Katz, 2016; Stein, 2018). The functional significance of different phases in the latter is readily apparent, as they for example provide alternating flexion and extension of limb joints, and coordination of movements between joints, limbs, and segments (Krantz and Parks, 2012; Grillner and El Manira, 2015; Kiehn, 2016; Le Gal et al., 2017; Bidaye et al., 2018). A hallmark of many such patterns is that the relative timing between neurons is well maintained over a range of rhythm frequencies (Dicaprio et al., 1997; Hooper, 1997b, a; Wenning et al., 2004; Marder et al., 2005; Grillner, 2006; Mullins et al., 2011; Le Gal et al., 2017). If the latency across different groups of neurons changes proportionally to the rhythm period, phase (latency over period) is invariant, in some cases providing optimal coordination at all speeds (Zhang et al., 2014).

The ability to maintain phase arises from central coordinating mechanisms between circuit elements, as it is present in isolated nervous system preparations, but the underlying cellular and circuit mechanisms are not well understood. Constant phase lags between neighboring segments in the control of swimming can be explained mathematically on the basis of asymmetrically weakly coupled oscillators, but the role of intrinsic and synaptic dynamics within each segment is unknown (Cohen et al., 1992; Skinner and Mulloney, 1998; Grillner, 2006; Mullins et al., 2011; Zhang et al., 2014; Le Gal et al., 2017).

The pyloric circuit of the crustacean stomatogastric ganglion (STG) has inspired a series of experimental and theoretical studies of cellular and synaptic mechanisms underlying phase maintenance. The pyloric circuit generates a triphasic motor pattern with stable phase relationships over a wide range of periods (Eisen and Marder, 1984; Hooper, 1997b, a; Bucher et al., 2005; Goaillard et al., 2009; Tang et al., 2012; Soofi et al., 2014). Follower neurons burst in rebound from inhibition from pacemaker neurons (Marder and Bucher, 2007; Daur et al., 2016), and post-inhibitory rebound delay scales with the period of hyperpolarizing currents (Hooper, 1998). Voltage-gated conductances slow enough for cumulative activation across cycles could promote such phase maintenance (Hooper et al., 2009). Similarly, short-term depression of graded inhibitory synapses is slow enough to accumulate over several pyloric cycles, meaning that effective synaptic strength increases with increasing cycle period (Manor et al., 1997; Nadim and Manor, 2000).

Theoretical studies have shown that short-term synaptic depression, by increasing inhibition strength with cycle period, should promote phase maintenance (Manor et al., 2003; Mouser et al., 2008), particularly in conjunction with inactivating (A-type) potassium currents (Bose et al., 2004; Greenberg and Manor, 2005), which control the rebound delay (Harris-Warrick et al., 1995b; Harris-Warrick et al., 1995a; Kloppenburg et al., 1999). These predictions remain experimentally untested.

Additionally, postsynaptic responses also depend on the actual trajectory of synaptic conductances, which are shaped by presynaptic voltage trajectories and short-term synaptic plasticity (Manor et al., 1997; Mamiya et al., 2003; Zhao et al., 2011; Tseng et al., 2014). If amplitude, duration, and trajectory of synaptic conductance determine rebound delay, phase maintenance necessitates all three of these parameters to change with cycle period in coordination. We used the dynamic

clamp technique to exhaustively explore the range of these parameters and understand how the coordinated changes in synaptic dynamics determines the phase of follower neurons in an oscillatory circuit. Our findings are consistent with a mathematical framework that accounts for the frequency dependence of amplitude and peak phase of the synaptic conductance.

Results

Phase maintenance and latency maintenance

The firing of neurons in oscillatory networks is shaped by a periodic synaptic input. The relative firing latency of such neurons is often measured relative to a defined reference time in each cycle of oscillation, and is used to determine the activity phase of the neuron (see, e.g., Belluscio et al., 2012). For example, in a simple network consisting of a bursting oscillatory neuron driving a follower neuron (Fig. 1A1), at a descriptive level, the latency (L) of the follower neuron activity relative to the onset of the oscillator's burst onset may depend on the oscillation cycle period (P). In response to a change in period (say, to P_2), the follower neuron may keep constant latency ($L_2 = L$), or constant phase, i.e., modify its latency proportionally to the change in period ($L_2/P_2 = L/P$; Fig. 1A2). However, in many oscillatory systems, for example the pyloric circuit (Hooper, 1997b, a), the relationship between L and P falls between these two extremes. A sample recording of the bursting activity of the lateral pyloric (LP) neuron in response to controlled changes in the pyloric cycle frequency demonstrates such a relationship (Fig. 1B and 1C).

The burst onset time of the isolated LP neuron depends on the temporal dynamics of its input

The LP neuron does not have intrinsic oscillatory properties, but oscillates due to the synaptic input it receives from the pacemaker anterior burster (AB) and pyloric dilator (PD) neurons, and the follower pyloric constrictor (PY) neurons (Fig. 2A). The burst onset phase of the LP neuron ($\varphi_{LP} = \Delta t / P$; Fig. 2A) is shaped by the interaction between synaptic inputs and the neuron's intrinsic dynamics that influence post-inhibitory rebound. We measured an overall burst onset phase of the LP neuron of φ_{LP} =0.34 ± 0.03 (N=9).

As a first-order quantification, we measured how inputs to the LP neuron interact with its intrinsic properties to determine the timing between its bursts, in the

absence of network oscillations. To this end, we synaptically isolated the LP neuron (Fig. 2B) and drove it with a noise current input (see Methods). In response to the noise input, the LP neuron produced an irregular pattern of spike times, which included a variety of bursting patterns with different spike numbers (Fig. 2C). We were interested in the characteristics of inputs producing different burst onset latencies. However, unlike a periodic input, noise input does not provide a well-defined reference point to measure the burst onset latency. We therefore categorized bursts with respect to the preceding inter-burst intervals (IBIs) during which no other action potentials occurred. We classified these IBIs in bins (300, 500, 700 and 900 ms) and tagged bursts based on the IBI values (Fig. 2C). We characterized the driving input leading to bursts with specific IBIs by burst-triggered averaging the input current (I_{BTA}; an example shown in Fig. 2D). Our analysis produced a single I_{BTA} for each of the four IBIs in each preparation (N=23). I_{BTA}'s of each preparation were first normalized in amplitude by the I_{BTA} amplitude at IBI = 300 ms (Fig. 2E; average shown in Fig. 2F) to examine how peak amplitude (I_{peak}) varied with IBI. These data were then normalized in time (Fig. 2G) to examine the effect of IBI on peak phase (Δ_{peak}) and the rise ($slope_{up}$) and fall ($slope_{down}$) slopes of the input current across preparations. We found that IBI had a significant effect on I_{peak}, Δ_{peak}, $slope_{up}$ and $slope_{down}$ (all one-way RM-ANOVA on ranks; data included in Figure 2-source data). In particular, larger IBIs corresponded to larger I_{peak} values (Fig. 2F-2H; $p<0.001$, $\chi^2 = 65.87$) with smaller (more advanced) Δ_{peak} (Fig. 2I; $p<0.001$, $\chi^2 = 41.35$). The change in Δ_{peak} was due to a decrease in $slope_{up}$ ($p<0.001$, $\chi^2 = 65.25$), whereas $slope_{down}$ did not vary as much (Figs. 2J-2K; $p=0.002$, $\chi^2 = 14.77$).

The burst onset phase of the LP neuron oscillation depends on its synaptic input

Injection of noise current revealed that the timing of the LP response is exquisitely sensitive to the duration and amplitude of inputs. In the intact system, the primary determinant of input duration and amplitude is the network period (P), as increasing P increases both presynaptic pacemaker burst duration (Hooper, 1997b, a) and synaptic strength (Manor et al., 1997; Nadim and Manor, 2000). To explore the effect of the duration and strength of the synaptic input, we used dynamic clamp to drive the LP neuron with a realistic synaptic conductance waveform.

We constructed this realistic waveform by measuring the synaptic current input to the LP neuron during ongoing pyloric oscillations (Fig. 3A). These measurements

showed the two components of inhibitory synaptic input, those from the pacemaker AB and PD neurons (left arrow) and those from the follower PY neurons (right arrow). In each cycle, the synaptic current always had a single peak, but the amplitude and phase of this peak showed variability across preparations (Fig. 3B, average in blue).

The realistic conductance input was injected periodically with strength g_{max} (Fig. 3C). For any fixed g_{max}, φ_{LP} decreased as a function of P (Fig. 3D), i.e., the relative onset of the LP burst was advanced in slower rhythms. In contrast to the effect of P, for any given P, φ_{LP} increased sublinearly as a function of g_{max} (Fig. 3E). Fig. 3F combines the simultaneous influence of both parameters on φ_{LP}. The results shown in Fig. 3D indicate that the LP neuron intrinsic properties alone do not produce phase constancy. However, level sets of φ_{LP} (highlighted for three values in Fig. 3F), indicate that phase could be maintained over a range of P values, if g_{max} increases as a function of P. This finding was predicted by our previous modeling work, in which we suggested that short-term synaptic depression promotes phase constancy by increasing synaptic strength as a function of P (Manor et al., 2003; Bose et al., 2004). We will further discuss the role of synaptic depression below.

To clarify the results of Fig. 3, it is worth examining the extent of phase maintenance for fixed g_{max}. An example of this is shown in Fig. 4A (turquoise plots). A comparison of these data with the theoretical cases in which either delay or phase is constant suggests that the LP neuron produces relatively good phase maintenance, at least much better in comparison with constant delay. However, this conclusion is misleading because, in these experiments, the duty cycle of the synaptic input was kept constant. Therefore, most of the phase maintenance is due the fact that the synaptic input keeps perfect phase. In fact, if the reference point measures phase relative to the end –rather than onset– of the PD burst (Fig. 4B), phase maintenance of the LP neuron is barely better than in the constant delay case (Fig. 4A, purple plots). It is therefore clear that phase maintenance by the LP neuron would require the properties of the synaptic input to change as a function of P, a hallmark of short-term synaptic plasticity (Fortune and Rose, 2001; Grande and Spain, 2005). As mentioned above, short-term plasticity such as depression could produce changes in g_{max} as a function of P. Independently of g_{max}, the peak time of the synaptic current is another parameter that could change with P and influence the timing of the postsynaptic burst.

We therefore proceeded to systematically explore the influence of P, g_{max} and the synaptic peak time on φ_{LP}.

A systematic exploration of synaptic input parameters on the phase of the LP neuron

For a detailed exploration of the influence of the synaptic input on φ_{LP}, we approximated the trajectory of the (unitary) synaptic conductance in one cycle by a simple triangle (Fig. 5A), which could be defined by three parameters: duration (T_{act}), peak time (t_{peak}) and amplitude (g_{max}) (Fig. 5B). This simplified triangular synaptic conductance waveform could then be repeated with any period (P) to mimic the realistic synaptic input to the LP neuron. For a given synaptic duration T_{act}, the peak phase of the synapse can be defined as $\Delta_{peak} = t_{peak} / T_{act}$). The parameter Δ_{peak} is known to vary as a function of P (Tseng et al., 2014) and, in a previous study, we found that Δ_{peak} may influence the activity of the postsynaptic neuron, independent of P and g_{max} (Mamiya and Nadim, 2004). We therefore systematically explored the influence of three parameters of the synaptic input (P, g_{max} and Δ_{peak}) on φ_{LP}.

As with the realistic synaptic waveforms (Fig. 3), we used the dynamic clamp technique to apply the triangular conductance waveform periodically to the synaptically isolated LP neuron. Across different runs within the same experiment, the parameters P, g_{max} and Δ_{peak} were changed on a grid (see Methods). In addition, all combinations of these three parameter values were run in two conditions in the same experiment, 1: with constant duration, i.e., constant T_{act} across different P values (C-Dur of 300 ms), and 2: with constant duty cycle, i.e., T_{act} changing proportionally to P (C-DC of 0.3; Fig. 5C). Using these protocols, we measured the effects of synaptic parameters on φ_{LP} (Fig. 5D).

The LP neuron produced burst responses that followed the synaptic input in a 1:1 manner across all values of P that were used (Fig. 6A1). When g_{max} and Δ_{peak} were kept constant, φ_{LP} decreased as a function of P (Fig. 6A2). This decrease was always larger for the C-Dur case than the C-DC case. For both C-DC and C-Dur, this trend was seen across all values of Δ_{peak} and g_{max} (Fig 6A3). The effect of P on φ_{LP} was highly significant for both C-DC (Three-Way ANOVA, $p<0.001$, $F=100.677$) and C-Dur (Three-Way ANOVA, $p<0.001$, $F=466.424$), indicating that the period and duration of the inhibitory input to the LP neuron had a significant effect on its phase.

Changing g_{max} produced a large effect on the level of hyperpolarization in the LP neuron, but this usually translated to only a small or modest effect on the time to the first spike following inhibition (Fig. 6B1). Overall, increasing g_{max} at constant values of P and Δ_{peak} produced a significant but only small to moderate increase in φ_{LP} (Three-Way ANOVA, $p<0.001$, $F=10.798$). Although increasing g_{max} produced the same qualitative effect for both the C-DC and C-Dur (e.g., Fig. 6B2), φ_{LP} in the C-DC case was restricted to a smaller range (Fig. 5F top vs. bottom panels). Overall, this increase was robust for most values of P and Δ_{peak} (Fig. 6B3).

Increasing Δ_{peak} for a constant value of P and g_{max} (Fig. 6C1), produced a small but significant increase in φ_{LP} (Three-Way ANOVA, $p<0.001$, $F=17.172$). This effect was robust for most values of P and g_{max}, for both C-DC and C-Dur (Fig. 6C2 and 6C3).

These results showed that all three parameters that define the shape of the IPSC influence φ_{LP}. Clearly, the strongest effect is the decrease in φ_{LP} as a function of P. However, φ_{LP} modestly increases as a function of the other two parameters, g_{max} and Δ_{peak}. This raised the question how g_{max} and Δ_{peak} would have to change in coordination as a function of P to counteract the effect of P on φ_{LP} and achieve phase constancy.

Coordinated changes of g_{max} and Δ_{peak} produce the largest effect on phase

To explore how g_{max} and Δ_{peak} might interact to influence φ_{LP}, we examined the sensitivity of φ_{LP} to these two parameters, individually and in combination, for all values of P in our data (see Methods). Sensitivity of φ_{LP} to these two parameters varied across P values, with larger sensitivity at lower values of P (data not shown; Two-Way RM-ANOVA, $p<0.001$, $F=16.054$). For simplicity, we averaged the sensitivity values across different P values to obtain an overall measure of the influence of g_{max} and Δ_{peak}. These results showed that, for the C-DC case, φ_{LP} had a positive sensitivity to g_{max} and a smaller positive sensitivity to Δ_{peak} (Fig. 7A). The sensitivity was largest if the two parameters were varied together ($g_{max} + \Delta_{peak}$) and smallest if they were varied in opposite directions ($g_{max} - \Delta_{peak}$; Two-Way RM-ANOVA, $p<0.001$, $F=3.330$). Similarly, these sensitivity values were also significantly different for the C-Dur case (Fig. 7B; Two-Way RM-ANOVA, $p<0.001$, $F=2.892$), with largest sensitivity for $g_{max} + \Delta_{peak}$ and smallest for $g_{max} - \Delta_{peak}$.

Level sets of φ_{LP} in the P-g_{max}-φ_{peak} space for C-DC and C-Dur cases

To search for phase constancy across different P values in our dataset, we expressed φ_{LP} as a function of the three IPSC parameters, P, g_{max} and Δ_{peak}: $\varphi_{LP} = \Phi(P, g_{\max}, \Delta_{peak})$. Figure 8 shows heat map plots of the function Φ, plotted for the range of values of P and Δ_{peak} and four values of g_{max}. In these plots, phase constancy can be seen as the set of values in each graph that are isochromatic, indicating the level sets of the function Φ. These level sets are mathematically defined as hypersurfaces on which the function has a constant value: $\Phi(P, g_{\max}, \Delta_{peak}) = \varphi_c$. For the C-DC case, in each g_{max} section of the plot, the level sets (e.g. φ_c = 0.34 denoted in white) spanned a moderate range of P values as Δ_{peak} increased (Fig. 8A1). The span of P values across all four panels indicates the range of cycle periods for which phase constancy could be achieved by varying g_{max} and Δ_{peak}. This range of P values (spanned by the white curves) was considerably smaller for the C-Dur case (Fig. 8A2).

For any constant phase value φ_c, these level sets can be expressed as

$$P = P_{\varphi_c}(g_{\max}, \Delta_{peak}),$$

which describes a surface in the 3D space, yielding the P value for which phase can be maintained at φ_c, for the given values of g_{max} and Δ_{peak}. The level set indicated by the white curves in panel A for the C-DC case is plotted as a heat map in Fig. 8B1 and can be compared with the same plot for the C-Dur case in Fig. 8B2. The range of colors in each plot (marked next to each panel) indicates the range of P values for which phase can be kept at φ_c = 0.34. To reveal how this range depends on the desired phase, we measured this range for all values of φ_c between 0.2 and 0.8 (Figs. 8C1 and 8C2). We found that the LP neuron could not achieve phases below 0.3 in the C-DC case (Fig. 8C1), which is simply because the neuron never fired during the inhibitory synaptic current (which had a duty cycle of 0.3). Furthermore, the range of P values for which the LP phase could be maintained by varying g_{max} and Δ_{peak} was much larger for C-DC inputs compared to C-Dur Inputs, for all φ_c values between 0.31 and 0.54.

A model of synaptic dynamics could predict activity onset phase of LP neuron

To gain a better understanding of our experimental results, we considered Equations (7) and (8)—the mathematical description of φ_{LP} as a function of P, g_{max} and Δ_{peak}, for the C-Dur and C-DC cases, respectively, that we derived in the Methods section—repeated here for convenience:

$$\varphi_{LP} = F(P, g_{max}, \Delta_{peak}) = \frac{\tau_s}{P} \ln \frac{g_{max}}{g^*} + \frac{\Delta_{peak} T_{act}}{P}, \quad (7)$$

$$\varphi_{LP} = F(P, g_{max}, \Delta_{peak}) = \frac{\tau_s}{P} \ln \frac{g_{max}}{g^*} + \Delta_{peak} DC. \quad (8)$$

In the C-Dur case, described by Equation (7), the input period has the most significant affect and φ_{LP} decays like $1/P$. In contrast, in the C-DC case, described by Equation (8), φ_{LP} is bounded from below by $\Delta_{peak} \cdot DC$ and thus behaves very differently than in the C-Dur case. In particular, as P increases, φ_{LP} approaches $\Delta_{peak} \cdot DC$ for the C-DC case, whereas it approaches 0 in the C-Dur case.

Keeping g_{max} (respectively, Δ_{peak}) constant in these equations allows us to obtain a relationship between P and Δ_{peak} (respectively, g_{max}), for which φ_{LP} is kept constant at φ_c. Consider Equations (7) and (8) for fixed values of both φ_{LP} (= φ_c) and g_{max}. Then these equations reduce to simple functional relationships where Δ_{peak} can be expressed as a function of P. In the C-DC case, for example, evaluating Δ_{peak} from Equation (8) produces

$$g_{max} = g^* \cdot \exp\left(\frac{P}{\tau_s} (\varphi_c - \Delta_{peak} DC) \right) \quad (1)$$

Equation (12) describes how g_{max} must vary with P for the system to maintain a constant phase φ_c for any given Δ_{peak}.

Alternatively, Δ_{peak} can be expressed as a function of P. In the C-DC case, evaluating Δ_{peak} from Equation (8) produces

$$\Delta_{peak} = \frac{\varphi_c}{DC} - \frac{\tau_s}{DC \cdot P} \ln \frac{g_{max}}{g^*}, \quad (2)$$

This equation describes how Δ_{peak} must vary with P for the system to maintain a constant phase φ_c for any given g_{max}. A comparison of these two cases can be seen in Fig. 9A, where either g_{max} (green) or Δ_{peak} (blue) is varied, while keeping the other parameter constant, to keep φ_{LP} constant at φ_c=0.34 across different P values. (The red curve is the depressing case, described below.) As the figure shows, phase constancy can be achieved by varying either parameter, but each parameter produces a different range of P across which phase is maintained.

In fact, Equation (13) can be used to calculate the range of P values over which changing Δ_{peak} (from 0 to 1) can maintain a constant phase φ_c. Solving $0 < \Delta_{peak} < 1$ using Equation (13) yields

$$\frac{\tau_s}{\varphi_c}\ln\frac{g_{max}}{g^*} < P_{DC} < \frac{\tau_s}{\varphi_c - DC}\ln\frac{g_{max}}{g^*} \quad (3)$$

Performing the same procedure in the C-Dur case, we find

$$\frac{\tau_s}{\varphi_c}\ln\frac{g_{max}}{g^*} < P_{Dur} < \frac{T_{act}}{\varphi_c} + \frac{\tau_s}{\varphi_c}\ln\frac{g_{max}}{g^*}. \quad (4)$$

If ΔP denotes the range of P values that respectively satisfy Equation (14) or (15), it is straightforward to show that $\Delta P_{DC} > \Delta P_{Dur}$ (compare black and blue curves in Fig. 9B and 9C). To see this, note that the lower bound for each interval is the same, thus we need to show that the upper bound for the C-DC case is larger than that for the C-Dur case. That is,

$$\varphi_c < DC\left(1 + \frac{\tau_s}{T_{act}}\ln\frac{g_{max}}{g^*}\right). \quad (5)$$

Equation (16) is true for τ_s and g_{max} large enough.

Two additional points are notable from Fig. 9B. First, the lower bound on φ_{LP} for which phase constancy can occur (i.e., φ_c) is smaller in the C-Dur than C-DC case. This is because we have assumed that in the C-DC case the LP neuron cannot fire during inhibition (i.e., until after Δ_{peak} DC). Second, for φ_c larger than ~ 0.5, ΔP is larger for the C-Dur case. This occurs because, when φ_c is sufficiently large, Equation (16) can no longer be satisfied. These findings are consistent with our experimental results described above, indicating that although phase constancy can be achieved when either g_{max} or Δ_{peak} increases with P, a concomitant increase of both—which could occur for example with a depressing synapse—greatly expands the range of P values for which a constant phase is maintained.

We now consider how short-term depression of the synapse—a property known to exist in the pacemaker to LP synapse (Zhao et al., 2011)—influences phase constancy by changing g_{max} and Δ_{peak}. We will restrict this section to the C-DC case. A similar derivation can be made for the C-Dur case. As mentioned in the Methods, the

effect of synaptic depression on synaptic strength can be obtained by Equation (11) (repeated from the Methods):

$$g_{max} = \bar{g}_{max} \cdot s_{max}(P) \tag{11}$$

where s_{max} is the maximum value of s_d at the onset of the pacemaker burst:

$$s_{max}(P) = \frac{1 - e^{-P(1-DC)/\tau_\alpha}}{1 - e^{-P(1-DC)/\tau_\alpha} e^{-DC \cdot P/\tau_\beta}}.$$

Note that s_{max} is a monotonically increasing function with values between 0 and 1. Its value approaches 1 as P increases, indicating that the synapse becomes stronger. In this equation, $\bar{g}_{max}$ is constant and is chosen so that the non-depressing and depressing conductances match at P = 1 s. As seen in Fig. 9A, when synaptic depression dictates how g_{max} varies with P as in Equation (11), and Δ_{peak} varies with P and g_{max} according to Equation (13), the simultaneous changes in g_{max} and Δ_{peak} (red) greatly increase the range of P values over which φ_{LP} is constant.

Returning to Fig. 9B, note that the C-DC case with depression spans a larger range of P values than the non-depressing case. Similarly, in Fig. 9C, the range of P values for which phase can be maintained is larger than the non-depressing case across φ_{LP} values, except where φ_{LP} is so large that the depressing synapse operates outside its dynamic range.

Discussion

The importance of phase in oscillatory networks

A common feature of oscillatory networks is that the activities of different neuron types are restricted to specific phases of the oscillation cycle. For example, different hippocampal and cortical neurons are active in at least three distinct phases of the gamma rhythm (Hajos et al., 2004; Hasenstaub et al., 2005), and distinct hippocampal neuron types fire at different phases of the theta rhythm and sharp wave-associated ripple episodes (Somogyi and Klausberger, 2005).

Experimental studies quantify the latency of neural activity with respect to a reference time in the cycle, but in most cases, these latencies are normalized and reported as phase. Distinct neuron types can maintain a coherent activity phase,

355 despite wide variations in the network frequency (30-100 Hz for gamma rhythms, 4-7
356 Hz for theta rhythms, and 120-200 Hz for sharp wave-associated ripple episodes).
357 Phase-specific activity of different neuron types is proposed to be important in rhythm
358 generation (Wang, 2010), and indicates the necessity of precise timing for producing
359 proper circuit output and behavior (Kopell et al., 2011). For example, phase locking of
360 spike patterns to oscillations is important for auditory processing, single cell and
361 network computations and Hebbian learning rules (Kayser et al., 2009; McLelland and
362 Paulsen, 2009; Panzeri et al., 2010). For brain oscillations, phase relationships may
363 provide clues about the underlying circuit connectivity and dynamics, but a behavioral
364 correlate of varying frequencies is not obvious. In contrast, the activity phase of distinct
365 neuron types in rhythmic motor circuits is a tangible readout of the timing of motor
366 neurons and muscle contractions, thus defining phases of movement (Grillner and El
367 Manira, 2015; Kiehn, 2016; Le Gal et al., 2017; Bidaye et al., 2018). Because
368 meaningful behavior depends crucially on proper activity phases, whether neurons
369 maintain their activity phase in face of changes in frequency simply translates to
370 whether the movement pattern changes as it speeds up or slows down.

371 *Determinants of phase*

372 In oscillatory networks, the activity phases of different neuron types depend to
373 different degrees on the precise timing and strength of their synaptic inputs (Oren et
374 al., 2006). Our results from noise current injections showed that the timing of the LP
375 neuron is strongly dependent on the timing of inputs it receives. Dynamic clamp
376 injection of realistic or triangular conductance waveforms with different periods (P)
377 indicated that φ_{LP} was largely determined by the duration of the synaptic input. φ_{LP}
378 changed substantially with P when inputs had constant duration, but much less when
379 inputs had a constant duty cycle, i.e., when duration scaled with P. However, our
380 experiments also showed that inputs of constant duty cycles alone are insufficient for
381 phase constancy. φ_{LP} decreased with P even with a constant duty cycle of inputs, but
382 increased with either synaptic strength (g_{max}) or peak phase of the synaptic input
383 (Δ_{peak}). The increase in φ_{LP} had similar sensitivity to g_{max} and Δ_{peak}, and therefore a
384 larger sensitivity to a simultaneous increase in both. Consequently, it was possible to
385 keep φ_{LP} constant over a wide range of cycle periods by increasing both parameters
386 with P.

The fact that an increase in g_{max} with P promotes phase constancy is biologically relevant, as short-term depression in pyloric synapses means that synaptic strength indeed increases with P (Manor et al., 1997). Previous modeling studies show that short-term synaptic depression of inhibitory synapses promotes phase constancy (Nadim et al., 2003; Bose et al., 2004), largely because of longer recovery times from depression at larger values of P.

The case is less clear for the finding that an increase of Δ_{peak} with P promotes phase maintenance, as we have previously shown that Δ_{peak} in LP actually decreases with P (Manor et al., 1997; Tseng et al., 2014). On the face of it, this suggests that an increase in Δ_{peak} is not a strategy employed in the intact circuit. However, the caveat is that such results may critically depend on the cause of the change in P, either technically and biologically. While in our current study we varied Δ_{peak} with direct conductance injection into LP, previous results were obtained by changing the waveform and period of the presynaptic pacemaker neurons. When P is changed in an individual preparation by injecting current into or voltage-clamping the pacemakers, phase of follower neurons is not particularly well maintained. An example of this is shown in Fig. 1, where φ_{LP} values fall between constant phase and constant duration and, additionally, all pyloric neurons show behavior that falls between constant phase and constant latencies (Hooper, 1997b, a). This may reflect that individuals are not keeping phase particularly well when the only cause of changing P is the presynaptic input. This is supported by the observation that even during normal ongoing pyloric activity, phases change with cycle-to-cycle variability of P in individual preparations (Bucher et al., 2005). However, it does not preclude the possibility that Δ_{peak} plays an important role in stable phase relationships when P differs because of temperature, neuromodulatory conditions, or inter-individual variability (discussed below).

It is noteworthy that a change in the synaptic strength or peak phase with P is not peculiar to graded synapses. The fact that short-term synaptic plasticity can act as a frequency-dependent gain control mechanism is well known for many spike-mediated synaptic connections. In bursting neurons, the presence of a combination of short-term depression and facilitation in the same spike-mediated synaptic interaction could also result in changes in the peak phase of the summated synaptic current as a function of burst frequency and duration, and the intra-burst spike rate (Markram et al., 1998).

Phase relationships in changing temperatures

An interesting case is provided by the observation that phases are remarkably constant when pyloric rhythm frequency is changed with temperature. Tang et al. (2012) report a 4-fold decrease in *P* of the pyloric rhythm between 7 and 23° C. In this study, none of the pyloric phases changed significantly, and it is worth noting that under conditions of changing temperatures, the relationships between *P*, g_{max}, and Δ_{peak} appeared to be fundamentally different from when *P* is changed at a constant temperature. Presynaptic voltage trajectories scaled with changing *P*, and Δ_{peak} of postsynaptic currents was independent of *P,* in contrast to the decrease described at constant temperature (Manor et al., 1997; Tseng et al., 2014). Amplitudes of synaptic potentials did not change with temperature, despite an increase in synaptic current amplitudes with increasing temperature (and associated decrease in *P*). This is in contrast to the positive relationship between g_{max} and *P* that results from synaptic depression at a constant temperature (Manor et al., 1997). Therefore, it appears that the likely substantial effects of temperature on synaptic dynamics and ion channel gating are subject to a set of compensatory adaptations different from when *P* is changed at constant temperature.

Slow compensatory regulation of phase

Phase maintenance in the face of changing *P* in an individual animal requires the appropriate short-term dynamics of synaptic and intrinsic neuronal properties. The fact that characteristic (and therefore similar) phase relationships can also be observed under the same experimental conditions across individual preparations is a different conundrum, particularly when *P* can vary substantially, as is true for brain oscillations (Hajos et al., 2004; Hasenstaub et al., 2005; Somogyi and Klausberger, 2005). Phases show different degrees of variability across individuals in a variety of systems, e.g., leech heartbeat (Wenning et al., 2018), larval crawling in *Drosophila* (Pulver et al., 2015), and fictive swimming in zebrafish (Masino and Fetcho, 2005), but in all of these cases phases are not correlated with *P*. In the pyloric rhythm, phases are also variable to a degree across individuals, but not correlated with the mean *P*, which varies >2-fold (Bucher et al., 2005; Goaillard et al., 2009). This phase constancy occurs despite considerable inter-individual variability in ionic currents, and is considered the ultimate target of slow compensatory regulation, i.e., homeostatic plasticity (Marder and Goaillard, 2006; Ma and LaMotte, 2007; Marder et al., 2014). Slow compensation can also be observed directly when rhythmic activity is disrupted by decentralization, and

453 subsequently recovers to similar phase relationships over the course of many hours
454 (Luther et al., 2003). It is interesting to speculate if our findings about how synaptic
455 parameters must change to keep phase constant would hold across individuals with
456 different mean *P*. The prediction would be coordinated positive correlations of both g_{max}
457 and Δ_{peak} with *P*.

458 *Phase relationships under different neuromodulatory conditions.*

459 The flipside of the question how neurons maintain phase is the question how
460 their phase can be changed. In motor systems in particular, changes in phase
461 relationships are functionally important to produce qualitatively different versions of
462 circuit output, for example to produce different gaits in locomotion (Vidal-Gadea et al.,
463 2011; Grillner and El Manira, 2015; Kiehn, 2016). The activity of neural circuits is
464 flexible, and much of this flexibility is provided by modulatory transmitters and
465 hormones which alter synaptic and intrinsic neuronal properties (Brezina, 2010; Harris-
466 Warrick, 2011; Jordan and Slawinska, 2011; Bargmann, 2012; Marder, 2012; Bucher
467 and Marder, 2013; Nadim and Bucher, 2014). The pyloric circuit is sensitive to a
468 plethora of small molecule transmitters and neuropeptides which affect cycle frequency
469 and phase relationships (Marder and Bucher, 2007; Stein, 2009; Daur et al., 2016).
470 With respect to our findings, any given neuromodulator could act presynaptically to
471 alter *P*, duration, or duty cycle on the one hand, and g_{max} and Δ_{peak} on the other. In
472 addition, the neuromodulator could affect the postsynaptic neuron's properties and
473 alter its sensitivity to any of these parameters. Therefore, our findings could not just
474 further our understanding of how phase can be maintained across different rhythm
475 frequencies, but also provide a framework for testing if and how changes in synaptic
476 dynamics may contribute to altering phase relationships under different
477 neuromodulatory conditions.

478 ## Materials and Methods

479 Adult male crabs (*Cancer borealis*) were acquired from local distributors and
480 maintained in aquaria filled with chilled (10-13°C) artificial sea water until use. Crabs
481 were prepared for dissection by placing them on ice for 30 minutes. The dissection was
482 performed using standard protocols as previously described (Tohidi and Nadim, 2009;
483 Tseng and Nadim, 2010). The STNS, including the four ganglia (esophageal ganglion,
484 two commissural ganglia, and the STG) and their connecting nerves, and the motor

485 nerves arising from the STG, were dissected from the stomach and pinned into a
486 Sylgard (Dow-Corning) lined Petri dish filled with chilled saline. The STG was
487 desheathed, exposing the somata of the neurons for intracellular impalement.
488 Preparations were superfused with chilled (10-13˚C) physiological *Cancer* saline
489 containing: 11 mM KCl, 440 mM NaCl, 13 mM $CaCl_2 \cdot 2H_2O$, 26 mM $MgCl_2 \cdot 6H_2O$,
490 11.2 mM Trizma base, 5.1 mM maleic acid with a pH of 7.4.

491 Extracellular recordings were obtained from identified motor nerves using
492 stainless steel electrodes, amplified using a differential AC amplifier (A-M Systems,
493 model 1700). One lead was placed inside a petroleum jelly well created to electrically
494 isolate a small section of the nerve, the other right outside of it. For intracellular
495 recordings, glass microelectrodes were prepared using the Flaming-Brown
496 micropipette puller (P97; Sutter Instruments) and filled with 0.6 M K_2SO_4 and 20 mM
497 KCl. Microelectrodes used for membrane potential recordings had resistances of 25-
498 30MΩ; those used for current injections had resistances of 15-22 MΩ. Intracellular
499 recordings were performed using Axoclamp 2B and 900A amplifiers (Molecular
500 Devices). Data were acquired using pClamp 10 software (Molecular Devices) and the
501 Netsuite software (Gotham Scientific), sampled at 4-5 kHz and saved on a PC using a
502 Digidata 1332A (Molecular Devices) or a PCI-6070-E data acquisition board (National
503 Instruments).

504 Individual pyloric neurons were impaled and identified via their membrane
505 potential waveforms, correspondence of spike patterns with extracellular nerve
506 recordings, and interactions with other neurons within the network (Weimann et al.,
507 1991).

508 *Constructing realistic IPSC waveforms*

509 Inhibitory postsynaptic currents (IPSCs) were recorded from LP neurons during
510 the ongoing rhythm using two-electrode voltage clamp and holding the LP neuron
511 at -50mV, far from the IPSC reversal potential of ~ -80 mV (Fig. 3A). When the LP
512 soma is voltage clamped at -50 mV, the axon (which is electrotonically distant from the
513 soma) can still produce action potentials following the synaptic inhibition from the
514 pacemaker neurons. The onset of the LP neuron action potentials (recorded in the
515 current trace) was used to calculate the mean IPSC for each experiment averaging the
516 IPSCs over 10-20 cycles. The IPSC waveforms were then extracted by normalizing
517 both the amplitude and the duration of the mean IPSC.

Driving the LP neuron with noise current

In these experiments, the preparation was superfused in *Cancer* saline plus 10^{-5} M picrotoxin (PTX; Sigma Aldrich) for 30 minutes to block the synaptic currents to the LP neuron. The removal of synaptic inhibition onto LP neurons changed the activity of these neurons from bursting to tonic firing. Then, noise current, generated by the Ornstein-Uhlenbeck process (Lindner), was injected into the isolated LP neurons for 60 minutes using the Scope software (available at http://stg.rutgers.edu/Resources.html,developed in the Nadim laboratory). The baseline of the noise current was adjusted by adding DC current so that it can provide enough inhibition to produce silent periods alternating with bursts of action potentials.

Driving the LP neuron with realistic or triangular IPSC waveforms in dynamic clamp

The dynamic clamp current was injected using the Netclamp software (Netsuite, Gotham Scientific). The synaptically isolated (10^{-5} M PTX) LP neuron was driven with an artificial synaptic current in dynamic clamp. The synaptic current was given as

$$I_{syn} = g_{syn}(V_{LP} - E_{syn})$$

where the synaptic conductance g_{syn} was a pre-determined waveform, repeated periodically with period P, and E_{syn} was the synaptic reversal potential set to −80 mV (Zhao et al., 2011).

Two sets of dynamic clamp experiments were performed on different animals. In one set of experiments, g_{syn} was set to be a triangular waveform. We measured the effects of four different parameters in these triangle conductance injections (Fig. 1): peak phase (Δ_{peak}), duration (T_{act}), period (P = time between onsets of dynamic clamp synaptic injections), and maximal conductance (g_{max}, the peak value of g_{syn}). This allowed us to explore which combinations of the different parameters influences the LP phase. Five values for P were used: 500, 750, 1000, 1500, and 2000 ms, which cover the typical range of pyloric cycle periods. Three values of g_{max} were used: 0.1, 0.2 and 0.4 μS, consistent with previous measurements of synaptic conductance (Zhao et al., 2011; Tseng et al., 2014). The value of Δ_{peak} was varied to be 0, 0.25, 0.5, 0.75 or 1. In the same experiment, all runs were done in two conditions: with T_{act} constant across different P values (C-Dur case with T_{act} = 300 ms) or with T_{act} changing proportionally to P (C-DC case with duty cycle $DC = T_{act}/P = 0.3$).

In the other set of experiments, g_{syn} was a realistic IPSC waveform, based on a pre-recorded IPSC in the LP neuron. In these experiments, P was varied to be 500, 750, 1000, 1250, 1500, or 2000 ms by scaling the realistic waveform in the time direction. In these experiments, g_{max} was set to be 0.1, 0.2, 0.4, 0.6, or 0.8 µS. The LP neuron burst onset delay (Δt) was measured relative to the onset of the pacemaker component of the synaptic input (identified by the kink in the synaptic conductance waveform) in each cycle. The burst phase was calculated as $\varphi_{LP} = \Delta t / P$. Phase constancy means that Δt changed proportionally to P. To measure the LP neuron phase with respect to the end of the pacemaker input, this reference used was the point on the synaptic conductance waveform marked by drawing a horizontal line from the kink that identified the onset of the pacemaker input.

Determining relationship between cycle period (P), synaptic strength (g_{max}) and LP phase (φ_{LP}) using the realistic IPSC waveform

We determined how well the mathematical model derived for constant input duty cycles (see Equation 8 below), matched the experimental data obtained with realistic IPSC waveforms. To this end, we fit the model to φ_{LP} values measured for all values of g_{max} and P, using the standard fitting routine 'fit' in MATLAB (Mathworks).

Sensitivity of φ_{LP} to g_{max} and Δ_{peak} across all P values

To explore how g_{max} and Δ_{peak} might interact to influence φ_{LP}, we first examined the sensitivity of φ_{LP} to these two parameters, individually and in combination, for all values of P in our data. For each cycle period, we computed the mean phase across all of our experiments (N=9) and all values of g_{max} (0.1, 0.2 and 0.4 µS) and we interpolated the φ_{LP} for g_{max} (0.2 and 0.4) to obtain φ_{LP} for 0.3 and Δ_{peak} (0, 0.25, 0.5, 0.75 or 1). This produced a 4 by 5 matrix of all of the values. For each data point in the matrix, we moved along eight different directions (increase both g_{max} and $\Delta_{peak,}$, increase g_{max}, increase $\Delta_{peak,}$, decrease both g_{max} and $\Delta_{peak,}$, decrease g_{max}, decrease Δ_{peak}, increase g_{max} and decrease Δ_{peak}, and decrease g_{max} and increase Δ_{peak}) and calculated the change in phase per unit (normalized) in $g_{max,}$ $\Delta_{peak,}$ or both.

A model of synaptic dynamics

In the derivation of the model, the firing time of the LP neuron was assumed to be completely determined by its synaptic input. This synaptic conductance (g_{syn}) was

assumed to rise and fall with distinct time constants. The following holds over one cycle period and therefore time is reset with period P (t (mod P)):

$$\frac{dg_{syn}}{dt} = \begin{cases} (g_{\max} - g_{syn})\tau_r & t \ (\mathrm{mod} P) < t_{peak} \\ -g_{syn} / \tau_s & t \ (\mathrm{mod} P) \geq t_{peak} \end{cases} \quad (6)$$

where the time t_{peak}, corresponding to Δ_{peak}, is $t_{peak} = \Delta_{peak} T_{act}$. We assumed that LP neuron remained inactive when g_{syn} was above a fixed threshold (g^*) less than g_{max}. Because the synaptic input is periodic with period P, we solved for the minimum and maximum values of g_{syn} in each cycle. The minimum (g_{lo}) occurred just before the onset (t = 0) of AB/PD activity, whereas the maximum occurred at the peak synaptic phase Δ_{peak} for the C-Dur case. In the C-DC case, $T_{act} = DC \cdot P$, where DC is the duty cycle (fixed at 0.3 in our experiments).

To calculate g^*, we set the value t = 0 so that $g_{syn}(0) = g_{lo}$ (and, by periodicity, $g_{syn}(P) = g_{lo}$), and solved the first part of Equation (1) where g_{syn} increases until $t = t_{peak}$. This yielded

$$g_{peak} = g_{syn}(t_{peak}) = g_{max} + (g_{lo} - g_{max})e^{-t_{peak}/\tau_r} \quad (7)$$

We then used the second part of Equation (1) to track the decay of g_{syn} for $t_{peak} < t < P$:

$$g_{syn}(t) = g_{peak} e^{-(t - t_{peak})/\tau_s} \quad (8)$$

Using Equation (3), we calculated the time Δt at which the synaptic conductance $g_{syn}(\Delta t) = g^*$ as follows:

$$g^* = g_{peak} e^{-(\Delta t - t_{peak})/\tau_s} \quad (9)$$

Solving Equation (4) for Δt yielded

$$\Delta t = \tau_s \ln \frac{g(t_{peak})}{g^*} + t_{peak}.$$

Dividing this equation by P yielded φ_{LP}:

$$\varphi_{LP} = F(P, g_{max}, \Delta_{peak}) = \frac{\tau_s}{P} \ln \frac{g_{peak}}{g^*} + \frac{t_{peak}}{P}, \quad (10)$$

where g_{peak} is given by Equation (2). This expression provides a description of the dependence of φ_{LP} as a function of P, g_{max} and Δ_{peak}. To explore the role of the parameters in this relationship, we made a simplifying assumption that the synaptic conductance $g_{syn}(t)$ rapidly reached its peak (i.e., τ_r was small), stayed at this value and started to decay at $t = t_{peak}$. In this case $g(t) = g_{max}$ on the interval $(0, t_{peak})$ and the value of g_{lo} is irrelevant. With this assumption, Equation (5) reduced to

$$\varphi_{LP} = \frac{\tau_s}{P} \ln \frac{g_{max}}{g^*} + \frac{t_{peak}}{P}. \tag{11}$$

Substituting $t_{peak} = \Delta_{peak} \cdot T_{act}$ in Equation (6), gave

$$\varphi_{LP} = F(P, g_{max}, \Delta_{peak}) = \frac{\tau_s}{P} \ln \frac{g_{max}}{g^*} + \frac{\Delta_{peak} T_{act}}{P}, \tag{12}$$

which we used to describe the LP phase in the C-Dur case. To describe the C-DC case, after substituting $t_{peak} = \Delta_{peak} \cdot DC \cdot P$, we obtained

$$\varphi_{LP} = F(P, g_{max}, \Delta_{peak}) = \frac{\tau_s}{P} \ln \frac{g_{max}}{g^*} + \Delta_{peak} DC. \tag{13}$$

Note that these equations also describe the relationship between φ_{LP} with T_{act} (or DC, in the C-DC case).

Equations (7) and (8) can be used to approximate a range of parameters over which φ_{LP} is maintained at a constant value. To do so, we assumed a specific parameter set, say $(\hat{P}, \hat{g}_{max}, \hat{\Delta}_{peak})$, satisfies

$$F(\hat{P}, \hat{g}_{max}, \hat{\Delta}_{peak}) = \hat{\varphi}_{LP},$$

for some fixed phase value, $\hat{\varphi}_{LP}$. We could now ask whether there are nearby parameters for which phase remains constant, i.e., F remains equal to $\hat{\varphi}_{LP}$. The Implicit Function Theorem (Krantz and Parks, 2012) guarantees that this is the case, provided certain derivatives evaluated at $(\hat{P}, \hat{g}_{max}, \hat{\Delta}_{peak})$ are non-zero, which turns out to be true over a large range of parameters. Since the partial derivative with respect to Δ_{peak} of $F(P, g_{max}, \Delta_{peak})$ at this point is a non-zero constant equal to T_{act}/P (or DC) in the C-Dur (or C-DC) case, there is a function $\Delta_{peak} = h(P, g_{max})$ such that

$$F(P, g_{max}, h(P, g_{max})) = \hat{\varphi}_{LP} \tag{14}$$

for values of P and g_{max} near $(\hat{P}, \hat{g}_{max})$. In other words, the Implicit Function Theorem guarantees that small changes in P and g_{max} can be compensated for by an appropriate choice of Δ_{peak} in order to maintain a constant LP phase. A similar analysis can be done by solving for g_{max} in terms of P and Δ_{peak} or by solving for P in terms of g_{max} and Δ_{peak}.

Adding synaptic depression to the model of synaptic dynamics

In a previous modeling study, we explored how the phase of a follower neuron was affected when the inhibitory synapse from an oscillatory neuron to this follower had short-term synaptic depression (Manor et al., 2003). In that study the role of the parameter Δ_{peak} was not considered. It is, however, straightforward to add synaptic depression to Equations (7) and (8).

An *ad hoc* model of synaptic depression can be made using a single variable s_d which will be a periodic function that denotes the extent of depression and takes on values between 0 and 1 (Bose et al., 2004). s_d decays during the AB/PD burst (from time 0 to T_{act}, indicating depression) and then recovers during the inter-burst interval (from T_{act} to P, indicating recovery). Thus, s_d can be described by an equation of the form:

$$\frac{ds_d}{dt} = \begin{cases} -s_d / \tau_\beta & t \pmod P \le T_{act} \\ (1 - s_d) / \tau_\alpha & T_{act} < t \pmod P < P \end{cases}$$

Using periodicity, it is straightforward to show that the maximum value of s_d, which occurs at the start of the AB/PD burst, is given by:

$$s_{max}(P) = \frac{1 - e^{-P(1-DC)/\tau_\alpha}}{1 - e^{-P(1-DC)/\tau_\alpha} e^{-DC \cdot P/\tau_\beta}}. \tag{15}$$

Note that s_{max} is a monotonically increasing function with values between 0 and 1. Its value approaches 1 as P increases, indicating that the synapse becomes stronger. For a complete derivation and description, see (Bose et al., 2004). The effect of synaptic depression on synaptic strength can be obtained by setting

$$g_{max} = \bar{g}_{max} \cdot s_{max}(P) \tag{16}$$

where s_{max} is given by Equation (10).

Software, analysis and statistics

Data were analyzed using MATLAB scripts to calculate the time of burst onset and the phase. Statistical analysis was performed using Sigmaplot 12.0 (Systat). Significance was evaluated with an α value of 0.05, error bars and error values reported denote standard error of the mean (SEM).

Acknowledgements

We thank Drs. Horacio Rotstein and Eric Fortune for helping with the initial MATLAB scripts in the analysis. This study was supported by NIH MH060605 and NSF DMS1122291.

Competing interests

The authors declare no competing financial interests.

References

Bargmann CI (2012) Beyond the connectome: how neuromodulators shape neural circuits. Bioessays 34:458-465.

Belluscio MA, Mizuseki K, Schmidt R, Kempter R, Buzsaki G (2012) Cross-frequency phase-phase coupling between theta and gamma oscillations in the hippocampus. J Neurosci 32:423-435.

Bidaye SS, Bockemuhl T, Buschges A (2018) Six-legged walking in insects: how CPGs, peripheral feedback, and descending signals generate coordinated and adaptive motor rhythms. J Neurophysiol 119:459-475.

Bose A, Manor Y, Nadim F (2004) The activity phase of postsynaptic neurons in a simplified rhythmic network. J Comput Neurosci 17:245-261.

Brezina V (2010) Beyond the wiring diagram: signalling through complex neuromodulator networks. Philos Trans R Soc Lond B Biol Sci 365:2363-2374.

Bucher D, Marder E (2013) SnapShot: Neuromodulation. Cell 155:482-482 e481.

Bucher D, Prinz AA, Marder E (2005) Animal-to-animal variability in motor pattern production in adults and during growth. J Neurosci 25:1611-1619.

Bucher D, Haspel G, Golowasch J, Nadim F (2015) Central Pattern Generators. eLS.

Buzsaki G, Wang XJ (2012) Mechanisms of gamma oscillations. Annu Rev Neurosci 35:203-225.

Buzsaki G, Tingley D (2018) Space and Time: The Hippocampus as a Sequence Generator. Trends in cognitive sciences 22:853-869.

689 Cohen AH, Ermentrout GB, Kiemel T, Kopell N, Sigvardt KA, Williams TL (1992)
690 Modeling of Intersegmental Coordination in the Lamprey Central Pattern
691 Generator for Locomotion. Trends in Neurosciences 15:434-438.
692 Daur N, Nadim F, Bucher D (2016) The complexity of small circuits: the
693 stomatogastric nervous system. Curr Opin Neurobiol 41:1-7.
694 Dicaprio R, Jordan G, Hampton T (1997) Maintenance of motor pattern phase
695 relationships in the ventilatory system of the crab. J Exp Biol 200:963-974.
696 Eisen JS, Marder E (1984) A mechanism for production of phase shifts in a pattern
697 generator. J Neurophysiol 51:1375-1393.
698 Fortune ES, Rose GJ (2001) Short-term synaptic plasticity as a temporal filter.
699 Trends Neurosci 24:381-385.
700 Goaillard JM, Taylor AL, Schulz DJ, Marder E (2009) Functional consequences of
701 animal-to-animal variation in circuit parameters. Nat Neurosci 12:1424-
702 1430.
703 Grande LA, Spain WJ (2005) Synaptic depression as a timing device. Physiology
704 (Bethesda, Md) 20:201-210.
705 Greenberg I, Manor Y (2005) Synaptic depression in conjunction with A-current
706 channels promote phase constancy in a rhythmic network. J Neurophysiol
707 93:656-677.
708 Grillner S (2006) Biological pattern generation: the cellular and computational
709 logic of networks in motion. Neuron 52:751-766.
710 Grillner S, El Manira A (2015) The intrinsic operation of the networks that make us
711 locomote. Curr Opin Neurobiol 31:244-249.
712 Hajos N, Palhalmi J, Mann EO, Nemeth B, Paulsen O, Freund TF (2004) Spike timing
713 of distinct types of GABAergic interneuron during hippocampal gamma
714 oscillations in vitro. J Neurosci 24:9127-9137.
715 Harris-Warrick RM (2011) Neuromodulation and flexibility in Central Pattern
716 Generator networks. Curr Opin Neurobiol 21:685-692.
717 Harris-Warrick RM, Coniglio LM, Levini RM, Gueron S, Guckenheimer J (1995a)
718 Dopamine modulation of two subthreshold currents produces phase shifts
719 in activity of an identified motoneuron. J Neurophysiol 74:1404-1420.
720 Harris-Warrick RM, Coniglio LM, Barazangi N, Guckenheimer J, Gueron S (1995b)
721 Dopamine modulation of transient potassium current evokes phase shifts in
722 a central pattern generator network. J Neurosci 15:342-358.
723 Hasenstaub A, Shu Y, Haider B, Kraushaar U, Duque A, McCormick DA (2005)
724 Inhibitory postsynaptic potentials carry synchronized frequency
725 information in active cortical networks. Neuron 47:423-435.
726 Hasselmo ME, Bodelon C, Wyble BP (2002) A proposed function for hippocampal
727 theta rhythm: separate phases of encoding and retrieval enhance reversal
728 of prior learning. Neural Comput 14:793-817.
729 Hooper SL (1997a) Phase maintenance in the pyloric pattern of the lobster
730 (Panulirus interruptus) stomatogastric ganglion. J Comput Neurosci 4:191-
731 205.
732 Hooper SL (1997b) The pyloric pattern of the lobster (Panulirus interruptus)
733 stomatogastric ganglion comprises two phase-maintaining subsets. J
734 Comput Neurosci 4:207-219.

735 Hooper SL (1998) Transduction of temporal patterns by single neurons. Nat
736 Neurosci 1:720-726.
737 Hooper SL, Buchman E, Weaver AL, Thuma JB, Hobbs KH (2009) Slow
738 conductances could underlie intrinsic phase-maintaining properties of
739 isolated lobster (Panulirus interruptus) pyloric neurons. J Neurosci
740 29:1834-1845.
741 Jordan LM, Slawinska U (2011) Chapter 12--modulation of rhythmic movement:
742 control of coordination. Prog Brain Res 188:181-195.
743 Katz PS (2016) Evolution of central pattern generators and rhythmic behaviours.
744 Philos Trans R Soc Lond B Biol Sci 371:20150057.
745 Kayser C, Montemurro MA, Logothetis NK, Panzeri S (2009) Spike-phase coding
746 boosts and stabilizes information carried by spatial and temporal spike
747 patterns. Neuron 61:597-608.
748 Kiehn O (2016) Decoding the organization of spinal circuits that control
749 locomotion. Nat Rev Neurosci 17:224-238.
750 Kloppenburg P, Levini RM, Harris-Warrick RM (1999) Dopamine modulates two
751 potassium currents and inhibits the intrinsic firing properties of an
752 identified motor neuron in a central pattern generator network. J
753 Neurophysiol 81:29-38.
754 Kopell N, Whittington MA, Kramer MA (2011) Neuronal assembly dynamics in the
755 beta1 frequency range permits short-term memory. Proc Natl Acad Sci U S
756 A 108:3779-3784.
757 Krantz SG, Parks HR (2012) The implicit function theorem: history, theory, and
758 applications: Springer Science & Business Media.
759 Le Gal JP, Dubuc R, Smarandache-Wellmann C (2017) Coordination of Rhythmic
760 Movements. In: Neurobiology of Motor Control: Fundamental Concepts and
761 New Directions (Hooper SL, Buschges A, eds). Hoboken, New Jersey: Wiley-
762 Blackwell.
763 Lindner B A brief introduction to some simple stochastic processes. Stochastic
764 Methods in Neuroscience 1.
765 Luther JA, Robie AA, Yarotsky J, Reina C, Marder E, Golowasch J (2003) Episodic
766 bouts of activity accompany recovery of rhythmic output by a
767 neuromodulator- and activity-deprived adult neural network. J
768 Neurophysiol 90:2720-2730.
769 Ma C, LaMotte RH (2007) Multiple sites for generation of ectopic spontaneous
770 activity in neurons of the chronically compressed dorsal root ganglion. J
771 Neurosci 27:14059-14068.
772 Mamiya A, Nadim F (2004) Dynamic interaction of oscillatory neurons coupled
773 with reciprocally inhibitory synapses acts to stabilize the rhythm period. J
774 Neurosci 24:5140-5150.
775 Mamiya A, Manor Y, Nadim F (2003) Short-term dynamics of a mixed chemical and
776 electrical synapse in a rhythmic network. J Neurosci 23:9557-9564.
777 Manor Y, Nadim F, Abbott LF, Marder E (1997) Temporal dynamics of graded
778 synaptic transmission in the lobster stomatogastric ganglion. J Neurosci
779 17:5610-5621.

780 Manor Y, Bose A, Booth V, Nadim F (2003) Contribution of synaptic depression to
781 phase maintenance in a model rhythmic network. J Neurophysiol 90:3513-
782 3528.
783 Marder E (2012) Neuromodulation of neuronal circuits: back to the future. Neuron
784 76:1-11.
785 Marder E, Bucher D (2001) Central pattern generators and the control of rhythmic
786 movements. Curr Biol 11:R986-996.
787 Marder E, Goaillard JM (2006) Variability, compensation and homeostasis in
788 neuron and network function. Nat Rev Neurosci 7:563-574.
789 Marder E, Bucher D (2007) Understanding circuit dynamics using the
790 stomatogastric nervous system of lobsters and crabs. Annu Rev Physiol
791 69:291-316.
792 Marder E, O'Leary T, Shruti S (2014) Neuromodulation of circuits with variable
793 parameters: single neurons and small circuits reveal principles of state-
794 dependent and robust neuromodulation. Annu Rev Neurosci 37:329-346.
795 Marder E, Bucher D, Schulz DJ, Taylor AL (2005) Invertebrate central pattern
796 generation moves along. Curr Biol 15:R685-699.
797 Markram H, Wang Y, Tsodyks M (1998) Differential signaling via the same axon of
798 neocortical pyramidal neurons. Proc Natl Acad Sci U S A 95:5323-5328.
799 Masino MA, Fetcho JR (2005) Fictive swimming motor patterns in wild type and
800 mutant larval zebrafish. J Neurophysiol 93:3177-3188.
801 McLelland D, Paulsen O (2009) Neuronal oscillations and the rate-to-phase
802 transform: mechanism, model and mutual information. J Physiol 587:769-
803 785.
804 Mouser C, Nadim F, Bose A (2008) Maintaining phase of the crustacean tri-phasic
805 pyloric rhythm. J Math Biol 57:161-181.
806 Mullins OJ, Hackett JT, Buchanan JT, Friesen WO (2011) Neuronal control of
807 swimming behavior: comparison of vertebrate and invertebrate model
808 systems. Prog Neurobiol 93:244-269.
809 Nadim F, Manor Y (2000) The role of short-term synaptic dynamics in motor
810 control. Curr Opin Neurobiol 10:683-690.
811 Nadim F, Bucher D (2014) Neuromodulation of neurons and synapses. Curr Opin
812 Neurobiol 29:48-56.
813 Nadim F, Booth V, Bose A, Manor Y (2003) Short-term synaptic dynamics promote
814 phase maintenance in multi-phasic rhythms. Neurocomputing 52-4:79-87.
815 Oren I, Mann EO, Paulsen O, Hajos N (2006) Synaptic currents in anatomically
816 identified CA3 neurons during hippocampal gamma oscillations in vitro. J
817 Neurosci 26:9923-9934.
818 Panzeri S, Brunel N, Logothetis NK, Kayser C (2010) Sensory neural codes using
819 multiplexed temporal scales. Trends Neurosci 33:111-120.
820 Pulver SR, Bayley TG, Taylor AL, Berni J, Bate M, Hedwig B (2015) Imaging fictive
821 locomotor patterns in larval Drosophila. J Neurophysiol 114:2564-2577.
822 Skinner FK, Mulloney B (1998) Intersegmental coordination in invertebrates and
823 vertebrates. Curr Opin Neurobiol 8:725-732.
824 Somogyi P, Klausberger T (2005) Defined types of cortical interneurone structure
825 space and spike timing in the hippocampus. J Physiol 562:9-26.

826 Soofi W, Goeritz ML, Kispersky TJ, Prinz AA, Marder E, Stein W (2014) Phase
827 maintenance in a rhythmic motor pattern during temperature changes in
828 vivo. J Neurophysiol 111:2603-2613.
829 Stein PSG (2018) Central pattern generators in the turtle spinal cord: selection
830 among the forms of motor behaviors. J Neurophysiol 119:422-440.
831 Stein W (2009) Modulation of stomatogastric rhythms. J Comp Physiol A
832 Neuroethol Sens Neural Behav Physiol 195:989-1009.
833 Tang LS, Taylor AL, Rinberg A, Marder E (2012) Robustness of a rhythmic circuit to
834 short- and long-term temperature changes. J Neurosci 32:10075-10085.
835 Tohidi V, Nadim F (2009) Membrane resonance in bursting pacemaker neurons of
836 an oscillatory network is correlated with network frequency. J Neurosci
837 29:6427-6435.
838 Tseng HA, Nadim F (2010) The membrane potential waveform of bursting
839 pacemaker neurons is a predictor of their preferred frequency and the
840 network cycle frequency. J Neurosci 30:10809-10819.
841 Tseng HA, Martinez D, Nadim F (2014) The frequency preference of neurons and
842 synapses in a recurrent oscillatory network. J Neurosci 34:12933-12945.
843 Vidal-Gadea A, Topper S, Young L, Crisp A, Kressin L, Elbel E, Maples T, Brauner M,
844 Erbguth K, Axelrod A, Gottschalk A, Siegel D, Pierce-Shimomura JT (2011)
845 Caenorhabditis elegans selects distinct crawling and swimming gaits via
846 dopamine and serotonin. Proc Natl Acad Sci U S A 108:17504-17509.
847 Wang XJ (2010) Neurophysiological and computational principles of cortical
848 rhythms in cognition. Physiol Rev 90:1195-1268.
849 Weimann JM, Meyrand P, Marder E (1991) Neurons that form multiple pattern
850 generators: identification and multiple activity patterns of gastric/pyloric
851 neurons in the crab stomatogastric system. J Neurophysiol 65:111-122.
852 Wenning A, Hill AA, Calabrese RL (2004) Heartbeat control in leeches. II. Fictive
853 motor pattern. J Neurophysiol 91:397-409.
854 Wenning A, Norris BJ, Gunay C, Kueh D, Calabrese RL (2018) Output variability
855 across animals and levels in a motor system. eLife 7.
856 Zhang C, Guy RD, Mulloney B, Zhang Q, Lewis TJ (2014) Neural mechanism of
857 optimal limb coordination in crustacean swimming. Proc Natl Acad Sci U S A
858 111:13840-13845.
859 Zhao S, Sheibanie AF, Oh M, Rabbah P, Nadim F (2011) Peptide neuromodulation of
860 synaptic dynamics in an oscillatory network. J Neurosci 31:13991-14004.

861

Figures

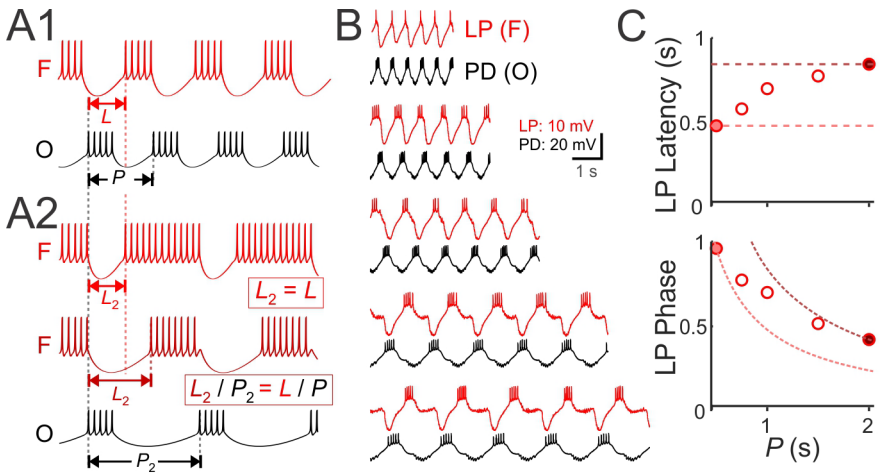

Figure 1: Latency constancy and phase constancy as a function of period

A1. Schematic diagram showing that a follower neuron (F) strongly inhibited by a bursting oscillatory neuron (O) with period *P* can produce rebound bursts with the same period at a latency *L*. **A2.** If the period of O changes to a new value (P_2), the new F burst latency (L_2) typically falls between two extremes: it could stay constant (top trace) or change proportionally to P_2, so that the burst phase (L / P) remains constant (middle trace). **B.** Example traces of the pyloric pacemaker PD neuron and the follower LP neuron represent the O and F relationship in panel A. Here, the PD neuron is voltage clamped and a pre-recorded waveform of the same neuron is used to force the neuron to follow different cycle periods. **C.** A measurement of the LP neuron burst onset phase with respect to the onset of the PD neuron burst shows that it falls between the two limits of constant latency and constant phase. Dotted curves represent constant latency matched to the latencies at the two extreme *P* values.

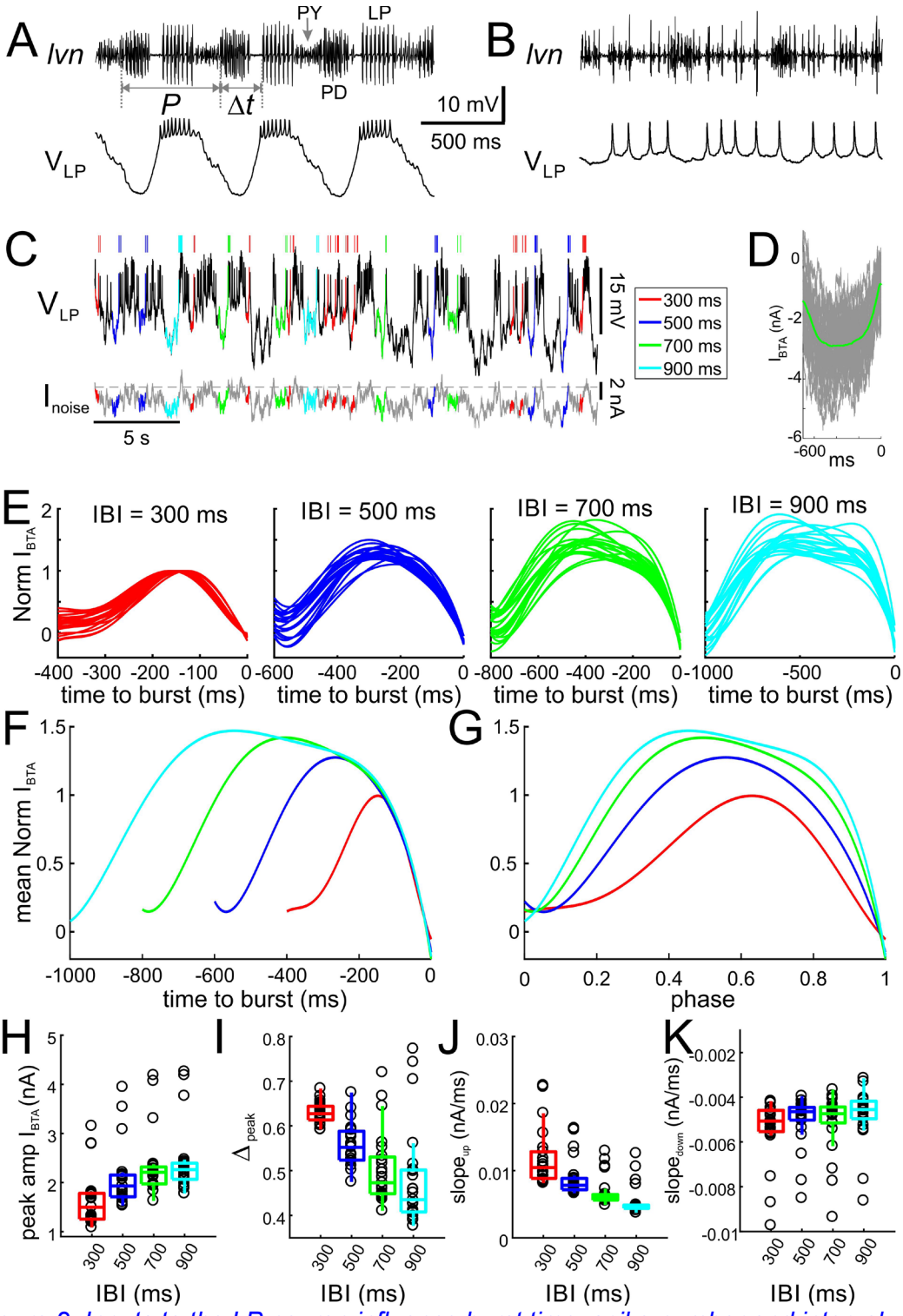

Figure 2: Inputs to the LP neuron influence burst time, spike number and interval

A. Simultaneous intracellular recording of the LP neuron and extracellular recording of the lateral ventricular nerve (*lvn*), containing the axons of the LP, PD and PY neurons (arrows). Period (*P*) and the burst onset time (*Δt*) of the LP neuron are defined in

reference to the pacemaker group (PD) burst. **B.** Blocking the synaptic inputs (10 μM picrotoxin) to the LP neuron disrupts its bursting oscillations. **C.** The synaptically isolated LP neuron was driven with a noise current input (I_{noise}) for 60 minutes. In response, the LP neuron produced an irregular pattern of bursting. Specific inter-burst intervals (*IBI*s) were tagged and used for burst-triggered averaging. **D.** Example of burst-trigger-averaged input current (I_{BTA}, green). Individual traces are shown in grey. **E.** For each *IBI* (300, 500, 700, 900 ms), I_{BTA} was calculated and normalized to the amplitude of I_{BTA} for *IBI*=300 ms. Different traces in each panel show the I_{BTA} of different preparations. **F.** The mean (across preparations) of the normalized I_{BTA}s shown in panel E. **G.** Traces in panel F normalized by *IBI*. **H-K.** Four parameters define the shape of the I_{BTA}: peak amplitude I_{amp} (**H**), peak phase Δ_{peak} (**I**), $slope_{up}$ (**J**) and $slope_{down}$ (**K**) across preparations. IBI had a significant effect on amplitude I_{amp} ($p<0.001$), peak phase Δ_{peak} ($p<0.001$), $slope_{up}$ ($p<0.001$) and $slope_{down}$ ($p=0.002$).

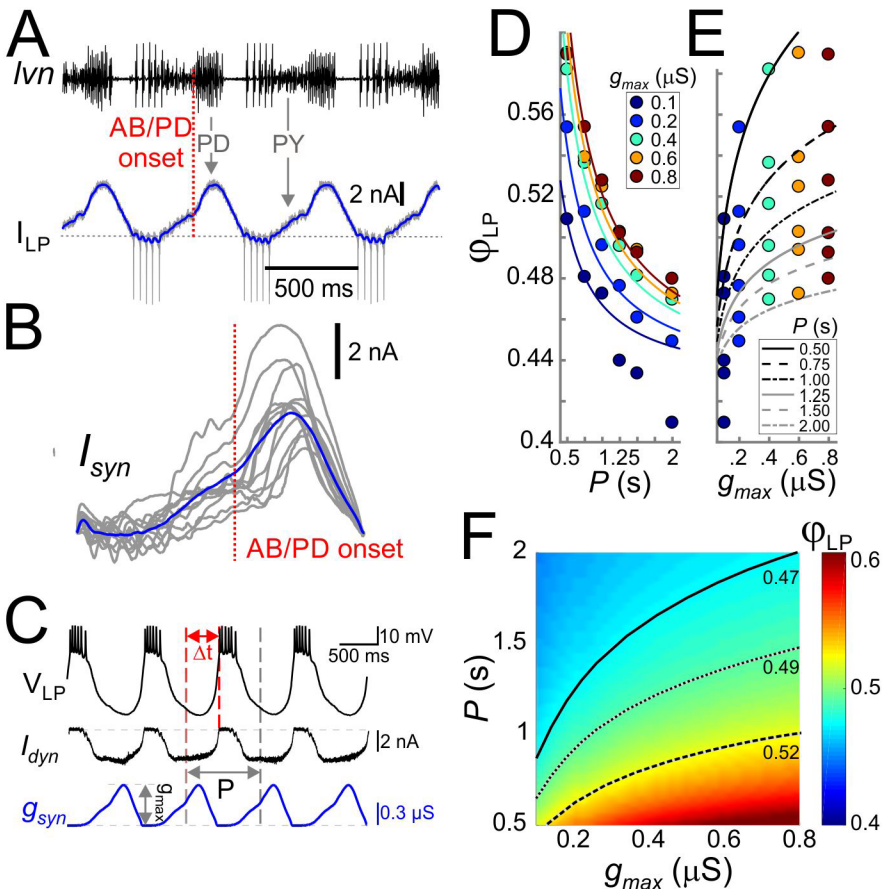

Figure 3: Cycle period and synaptic strength affect the phase of LP burst onset in opposite directions.

A. The synaptic input to the LP neuron was measured by voltage clamping it at a holding potential of -50mV during ongoing oscillations. The onset of the pacemaker (AB/PD) activity is seen as a kink in the synaptic current (I_{LP}, blue). **B.** Synaptic input averaged across cycles from 9 different LP neurons. The blue trace shows the average. **C.** An example of the LP neuron driven by the realistic synaptic waveform in dynamic clamp. The burst onset time (Dt) was measured relative to the AB/PD onset and used to measure the LP phase (φ_{LP}). g_{max} denotes the conductance amplitude. **D.** Mean φ_{LP} (N=9 preparations) shown as a function of P and fit with the function given by Equation (8) (fit values τ_s = 26.0 ms, g^* = 0.021 µS and $\Delta_{peak} \cdot DC$ = 0.43). **E.** Mean φ_{LP} plotted against g_{max} also shown with the fit to Equation (8). **F.** Heat map, obtained from fitting Equation (8) to the data in panels D and E, shows φ_{LP} as a function of both g_{max} and P. Black curves show the level sets of phase constancy for three values of φ_{LP} (0.47, 0.49, and 0.52).

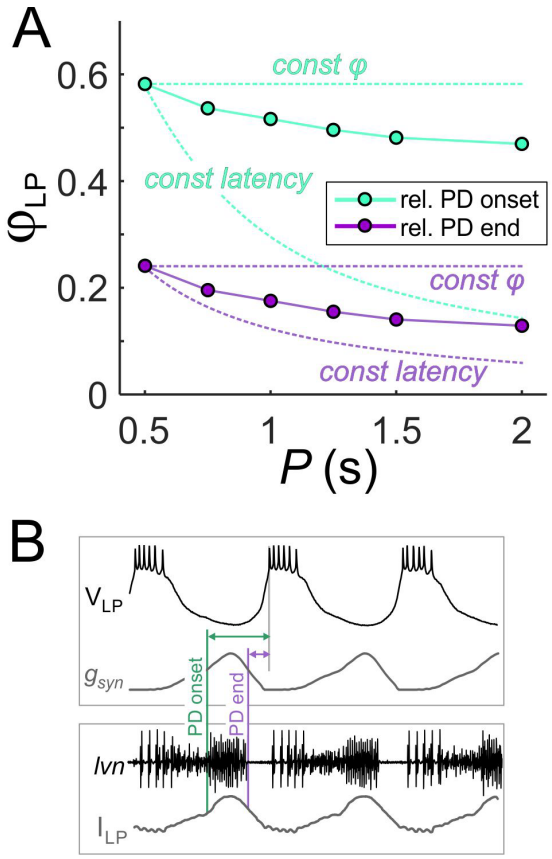

911

912 *Figure 4: The constant duty cycle of synaptic conductance is a major factor in phase*
913 *maintenance.*

914 **A.** The change in φ_{LP} values with P are compared with the constant phase (solid curve)
915 and constant duration (dashed curve) extremes. Lime traces show the usual values of
916 φ_{LP}, calculated from the LP burst onset latency with respect to the onset of the PD
917 burst. Lavender traces show φ_{LP} calculated from the LP burst onset latency with
918 respect to the end of the PD burst. Data shown are the same as in Fig. 3D for g_{max}=0.4
919 µS. **B.** Schematic diagram shows the latency of LP burst onset measured with respect
920 to the (estimated) onset and end of the PD burst in the dynamic clamp experiments
921 (see Methods). Bottom panel shows the synaptic current waveform measured in the
922 voltage-clamped LP neuron during ongoing pyloric activity. Top panel shows the
923 dynamic clamp injection of the synaptic conductance waveform into a synaptically-
924 isolated LP neuron. The current waveform of the bottom panel is aligned to the
925 conductance waveform of the top panel for the comparison used in determining the PD
926 burst onset and end in the top panel.

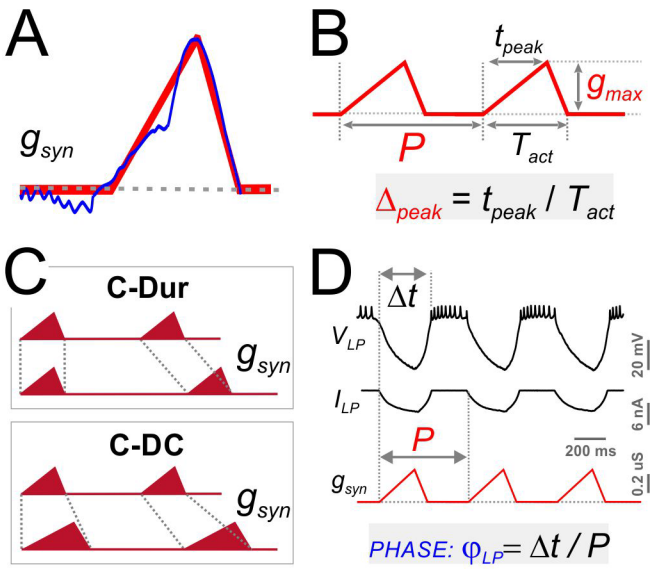

Figure 5: Four parameters describing synaptic shape were varied in the experimental paradigm.

A. A triangle shaped conductance was used to mimic the synaptic input to the LP neuron. **B.** The triangular waveform can be described by period (P), duration (T_{act}), peak time (t_{peak}) and amplitude (g_{max}). **C.** In dynamic clamp runs, the synapse duration T_{act} was kept constant at 300 ms (C-Dur) or maintained at a constant duty cycle (T_{act} /P) of 0.3 (C-DC) across all values of P. **D.** Intracellular voltage recording of the synaptically isolated LP neuron during a dynamic clamp stimulation run using the triangle conductance. The burst onset time (Δt, calculated in reference to the synaptic conductance onset) was used to calculate the activity phase ($\varphi_{LP} = \Delta t/P$).

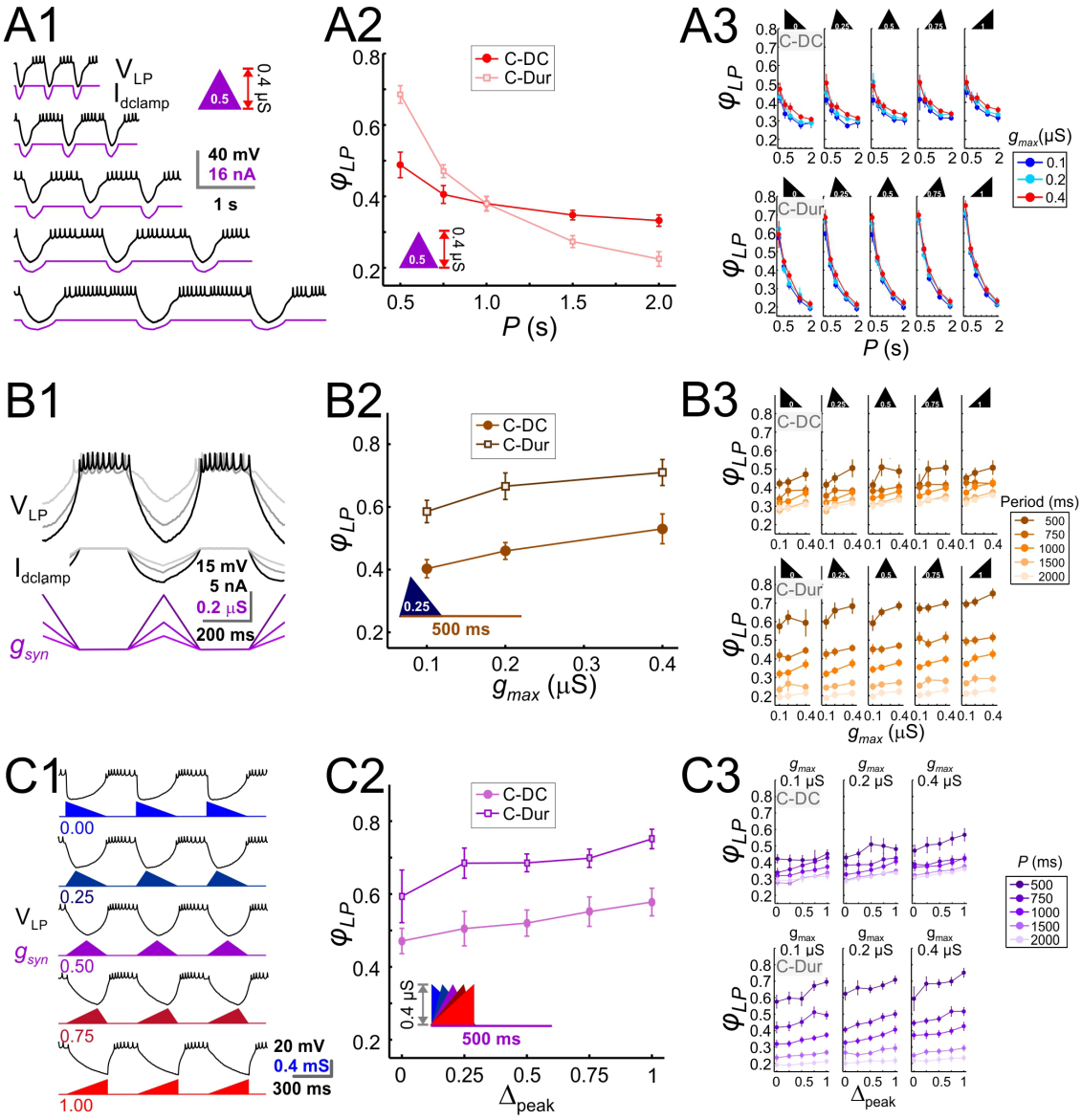

Figure 6: The LP burst onset phase decreases as a function of P, but increases as a function of g_{max} and Δ_{peak}.

Periodic injection of an inhibitory triangular waveform conductance into the isolated LP neuron produced bursting activity from which φ_{LP} was calculated. The parameters g_{max}, Δ_{peak} and P were varied across runs for both C-Dur and C-DC cases. **A.** φ_{LP} decreases as a function of P. **A1.** Intracellular recording of an LP neuron showing a C-DC conductance input across five periods. **A2.** φ_{LP} for the example shown in A1 plotted as a function of P (for g_{max} = 0.4 µS, Δ_{peak} = 0.5) for both C-Dur and C-DC cases. φ_{LP} decreases rapidly with P and the drop is larger for the C-Dur case. **A3.** φ_{LP} decreased with P in both the C-DC case (Three-Way RM ANOVA, p<0.001, F=100.7) and the C-Dur case (Three-Way RM ANOVA, p<0.001, F=466.4) and all values of Δ_{peak}. The

range of φ_{LP} drop was greater for the C-Dur case compared to the C-DC case. **B.** φ_{LP} increases as a function of g_{max}. **B1.** Intracellular recording of an LP neuron showing the conductance input across three values of g_{max}. **B2.** φ_{LP} for the example shown in B1 plotted as a function of P (for P = 500 ms, Δ_{peak} = 0.25) shows a small increase for both C-Dur and C-DC cases. **B3.** φ_{LP} increased with g_{max} in almost all trials for both C-DC and C-Dur cases and all values of Δ_{peak}. **C.** φ_{LP} increases as a function of Δ_{peak}. **C1.** Intracellular recording of the LP neuron showing the conductance input for five values of Δ_{peak}. **C2.** φ_{LP} for the example neuron in C1 plotted as a function of Δ_{peak} (for P = 500 ms, g_{max} = 0.4 µS) for both C-DC and C-Dur cases. **C3.** φ_{LP} increased with Δ_{peak} for both C-DC and C-Dur cases and all values of g_{max}.

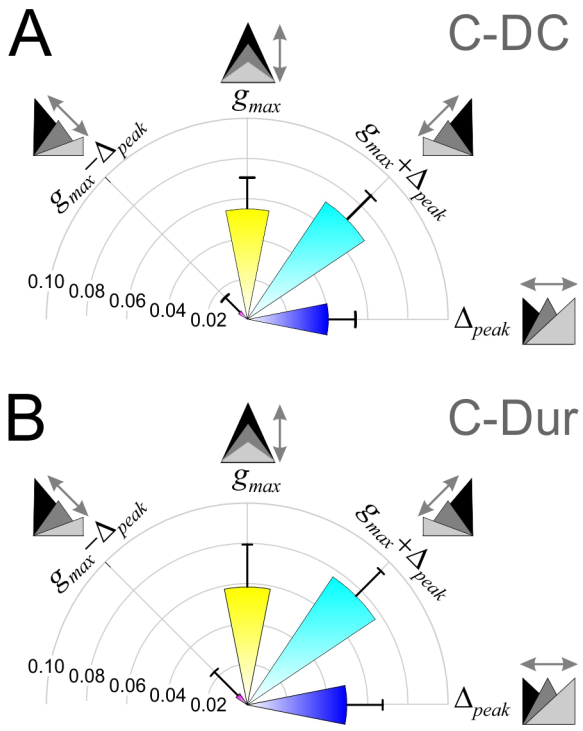

Figure 7: Sensitivity analysis shows that φ_{LP} increases more effectively if g_{max} and Δ_{peak} increase together.

A. The sensitivity φ_{LP} to local changes in g_{max} and Δ_{peak} was averaged across all values of P for the C-DC case. The sensitivity was largest if both parameters were increased together (g_{max} + Δ_{peak}) and smallest if they were varied in opposite directions (g_{max} - Δ_{peak}; One-Way RM-ANOVA, $p<0.001$, $F=3.330$). **B**. The same sensitivity analysis in the C-Dur case shows similar results (One-Way RM-ANOVA, $p<0.001$, $F=2.892$).

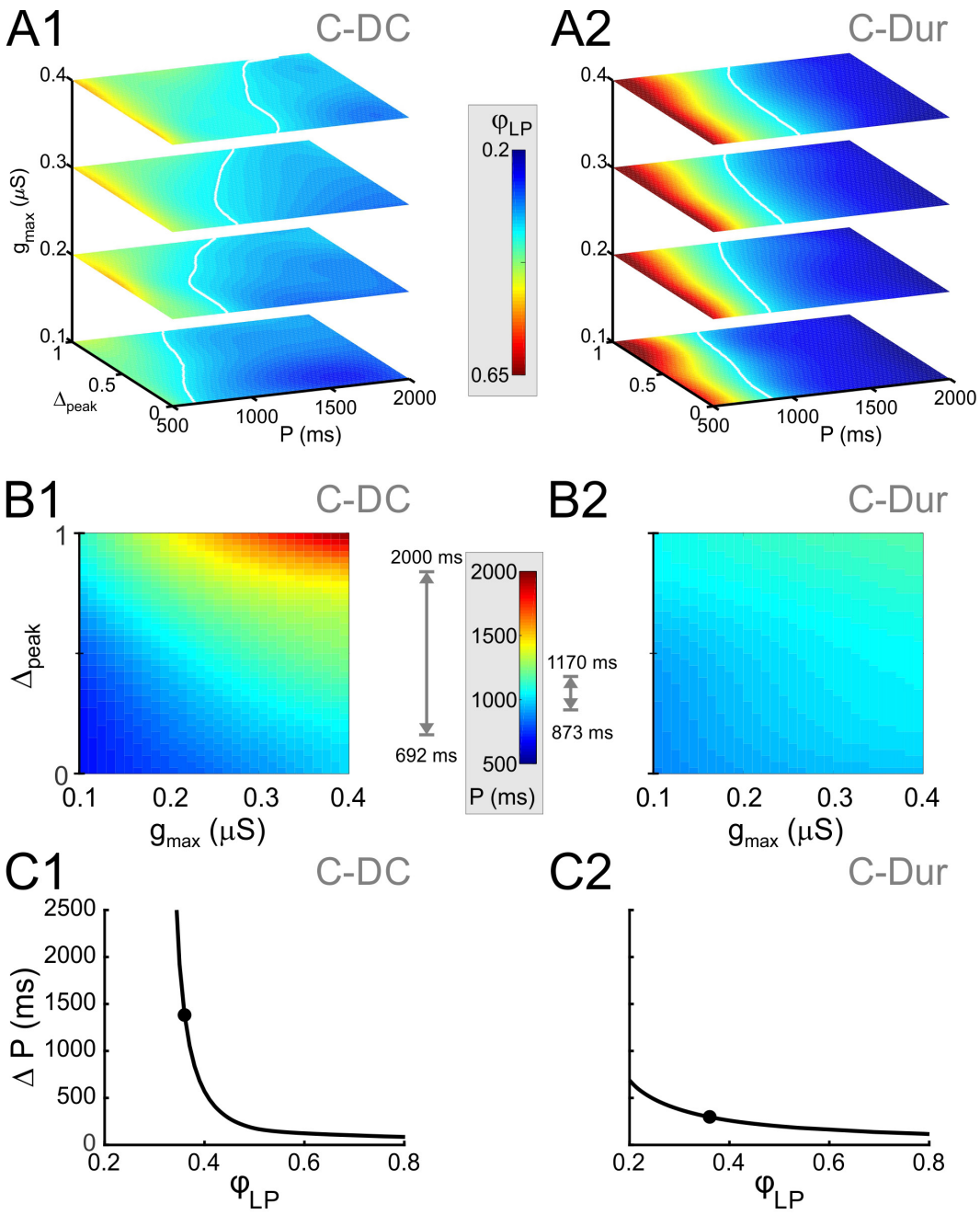

Figure 8: Simultaneous increase of both Δ_{peak} and g_{max} across their range of values can produce phase maintenance across a large P range in the C-DC case and a much smaller P range in the C-Dur case

A. Heat map plots of the function Φ, plotted for the range of values of *P* and Δ_{peak} and 4 values of g_{max} for the C-DC (**A1**) and C-Dur (**A2**) cases. The white curves show the level set of φ_{LP} = 0.34, shown as an example of phase constancy. The color maps are interpolated from sampled data (see Methods; N=9) **B.** Heat map for the level sets φ_{LP} = 0.34 for the C-DC (**B1**) and C-Dur (**B2**) cases. Range of colors in each panel indicate

977 the range of *P* values for which φ_{LP} could remain constant at 0.34 for each case, as
978 indicated by the grey arrows on the side of the heatmap color legend. **C.** The range
979 (ΔP) of *P* values for which φ_{LP} could remain constant at any value between 0.2 and 0.8
980 for the C-DC (**C1**) and C-Dur cases (**C2**). Filled circles show the values shown in panel
981 B. The LP neuron cannot achieve φ_{LP} values below 0.3 in the C-DC case. For φ_{LP}
982 values between 0.3 and ~0.65, the range was larger in C-DC case.

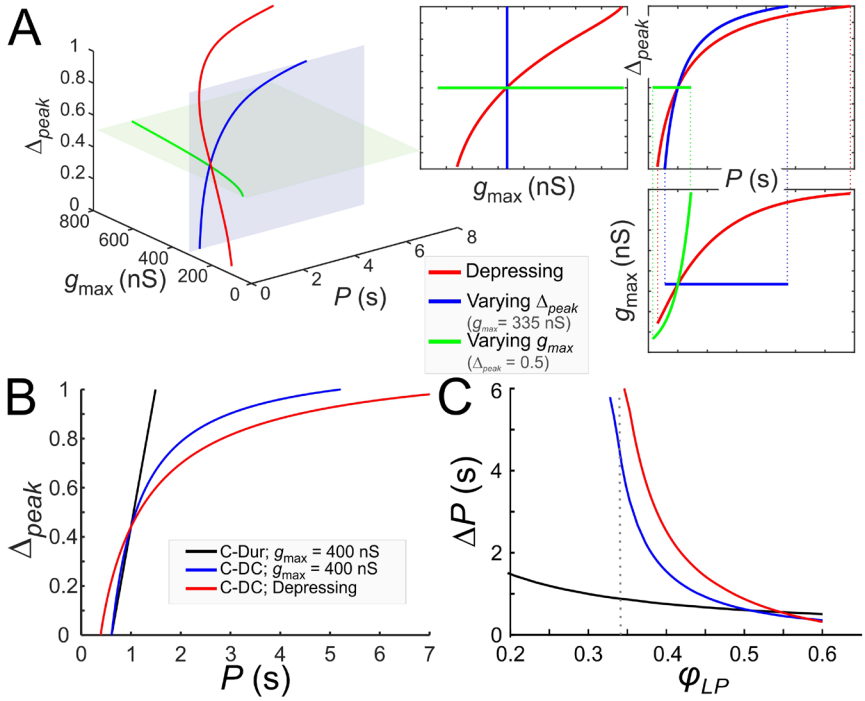

Figure 9: Model prediction of the range of phase constancy.

A. For the C-DC case, a constant phase of φ_{LP} = 0.34 can be maintained across a range of cycle periods P when g_{max} is constant (at 335 nS; blue plane) and Δ_{peak} varies from 0 to 1 according to Equation (13) (blue), or when Δ_{peak} is fixed (at 0.5; green plane) and g_{max} varies from 200 to 800 nS according to Equation (12). Alternatively, g_{max} and Δ_{peak} can covary to maintain phase, as in a depressing synapse, where g_{max} varies with P according to Equation (11), and Δ_{peak} is calculated for each P and g_{max} value according to Equation (13). As seen in the 2D coordinate-plane projections of the 3D graph (right three graphs), the range of P values for which phase constancy is achieved is largest when g_{max} and Δ_{peak} covary (dotted lines show limits of P for phase constancy). The depressing synapse conductance is chosen to be 335 nS at P = 1 s. **B, C.** A comparison between the C-DC and C-Dur cases shows that in the latter case a constant phase of φ_{LP} can be maintained across a larger range of P values when Δ_{peak} increases with P (and g_{max} is fixed at 400 nS) according to Equation (13). The relationship of Δ_{peak} and P is shown in **B** for φ_{LP} = 0.34. **C** shows the range of P values (ΔP) of cycle periods for which phase remains constant at φ_{LP}. If g_{max} also varies with P, as in a depressing synapse (red; Equation (11)), the range of P values for which phase is constant is further increased. (Dotted line: φ_{LP} = 0.34.)

Source Data Files

Figure 2-1. *File: Figure2_sourcedata.xlsx*

This Excel file contains 4 sheets, including all measured attributes of the burst-triggered average current (I_{BTA}) for different IBIs (N=23) as shown in Fig. 2H-2K.